Research Square

Preprints are preliminary reports that have not undergone peer review.
They should not be considered conclusive, used to inform clinical practice,
or referenced by the media as validated information.

Multiscale Thermal Transport in AlPO-18 for Heat-Transformation Applications

Mahdi Mourad LAICHAOUI

LaichaouiMahdiMourad@gmail.com

Nanjing University of Aeronautics and Astronautics

Zhaofeng Chen

Nanjing University of Aeronautics and Astronautics

Rami Mrad

University of Science and Technology of China

. Ayesha

Nanjing University of Aeronautics and Astronautics

Article

Keywords: AlPO-18, AEI framework, negative thermal expansion, lattice dynamics, thermal transport, deviational Monte Carlo

Posted Date: November 13th, 2026

DOI: https://doi.org/10.21203/rs.3.rs-10956470/v1

License: This work is licensed under a Creative Commons Attribution 4.0 International License.
Read Full License

Additional Declarations: No competing interests reported.

Multiscale Thermal Transport in AlPO-18 for Heat-Transformation Applications

Abstract

A multiscale analysis of framework dynamics, negative thermal expansion, and heat transport is presented for AlPO-18, with explicit distinction between crystallographic cell conventions and transport operators. The calcined conventional C2/c cell contains $Al_{24}P_{24}O_{96}$, 144 atoms, and has a volume of 3241.81 Å³, whereas the corresponding 72-atom primitive cell has a volume of 1620.90 Å³. The calculated elastic tensor is positive definite, with stiffness eigenvalues ranging from 13.9 to 222 GPa. The Reuss bulk, shear, and Young moduli are 73.56, 19.34, and 53.35 GPa, respectively. Variable-temperature diffraction reveals a volume contraction of 0.91% between 105 and 455 K. The volumetric thermal-expansion coefficient remains negative throughout this interval, changing from -30.75×10^{-6} K^{-1} at 105 K to -22.41×10^{-6} K^{-1} at 455 K, with a value of -26.18×10^{-6} K^{-1} at 298 K. No thermal-expansion crossover is observed. Analysis of the local T···T distances and the eight-membered-ring span shows that the contraction is governed primarily by transverse Al–O–P hinging and cooperative tetrahedral rotations rather than uniform bond shortening. A 216-branch harmonic spectrum, Raman comparison, charge-density redistribution, and heat-capacity-weighted mode analysis associate this structural flexibility with low-frequency collective framework vibrations. The transport analysis distinguishes three physically different conductivity baselines: 1.150 W m^{-1} K^{-1} for the periodic Wigner total, 0.773 W m^{-1} K^{-1} for the reservoir Monte Carlo population target, and 0.370 W m^{-1} K^{-1} for the boundary-limited platelet response. These values correspond to different operators, geometries, and channel definitions and therefore do not represent competing estimates of a single bulk conductivity. A gray two-stream benchmark gives a statistical convergence slope of −0.53 and approaches the diffusive limit within 2% for $L/\Lambda \geq 98$. Boundary calculations and AlPO-18/PVOH coating transients further demonstrate how thickness, surface specularity, and coupled heat and mass transfer modify the intrinsic framework response. The study establishes a quantitatively consistent connection between cell normalization, macroscopic contraction, framework vibrations, transport channels, and application-scale thermal behaviour in AlPO-18.

Keywords: AlPO-18; AEI framework; negative thermal expansion; lattice dynamics; thermal transport; deviational Monte Carlo

1. Introduction

Microporous aluminophosphates are charge-neutral frameworks constructed from alternating AlO_4 and PO_4 tetrahedra. Their interconnected cages and channels make them useful for adsorption, molecular separation, catalysis, and thermally driven energy-conversion processes [1–5]. AlPO-18 is a representative material of the AEI framework topology. Its calcined structure contains a three-dimensional network of eight-membered-ring channels with an effective aperture of approximately 3.8 Å and a framework density of about 15 tetrahedral atoms per 1000 Å³ [6,7]. Strong Al–O and P–O bonds preserve the integrity of the tetrahedra, whereas variations in the Al–O–P angles and cooperative rotations of adjacent tetrahedra provide more flexible structural degrees of freedom. These low-energy angular motions influence both the thermal expansion of the framework and the transport of vibrational energy. Framework flexibility can produce negative thermal expansion, but the macroscopic response cannot be established from a limited number of negative mode-Grüneisen parameters. The volumetric thermal-expansion coefficient, $\alpha_V(T)$, depends on the heat-capacity-weighted contributions of the complete vibrational spectrum and must be determined from a quasiharmonic calculation or from the temperature derivative of the unit-cell volume [8–11]. Variable-temperature diffraction measurements have shown that AlPO-18 contracts between approximately 110 and 450 K and have related this behaviour to structural units shared by the AEI and CHA framework topologies [12]. A complete interpretation therefore requires three complementary results: the temperature-dependent volumetric coefficient, the local structural changes responsible for contraction, and the vibrational modes associated with those changes. The same low-frequency framework motions also affect thermal transport. Weakly dispersive optical modes have small group velocities and therefore carry limited population heat current. Anharmonic broadening can additionally produce spectral overlap between neighbouring modes, allowing a coherence contribution to thermal transport. The Wigner formulation describes these effects by separating the lattice thermal conductivity into population and coherence channels [13–16]. Conductivities obtained using different transport formalisms, however, cannot be compared directly unless they employ the same modal properties, crystallographic direction, scattering operator,

boundary conditions, and channel definition. A periodic Wigner conductivity, a reservoir-driven Monte Carlo result, and a boundary-limited platelet conductivity consequently represent different transport conditions rather than three estimates of the same bulk quantity. Previous investigations of AlPO-18 have reported the calcined C2/c crystal structure [6], temperature-dependent lattice contraction [12], first-principles elastic properties [17], Raman-active framework vibrations [18], powder morphology and diffraction characteristics [19], and the transient thermal response of AlPO-18/PVOH coatings [20]. These studies provide important information at different length scales, but their results have not been combined into a consistent description of framework dynamics, thermal expansion, and heat transport. Direct comparison is further complicated by the different crystallographic cells used in the literature. The 144-atom C-centred conventional cell has twice the volume of the 72-atom primitive cell, while the average Cmcm structure used for variable-temperature refinement differs from the lower-symmetry calcined C2/c structure.

In the present work, each volume-dependent quantity is assigned to an explicitly defined 144- or 72-atom cell, thereby removing the ambiguity in the reported equilibrium volume. The macroscopic thermal response is established by calculating $\alpha_V(T)$ from the fitted unit-cell volume and comparing it with the directional expansion coefficients, local T···T distances, eight-membered-ring contraction, and heat-capacity-weighted mode contributions. The periodic Wigner, reservoir Monte Carlo, and platelet conductivity values are then reconciled by identifying the transport operator, geometry, direction, and channel content associated with each result. Harmonic phonon dispersion, vibrational density of states, Raman activity, charge redistribution, Monte Carlo convergence, boundary suppression, and coating transients are finally combined to connect atomic-scale framework flexibility with thermal transport across progressively larger length scales.

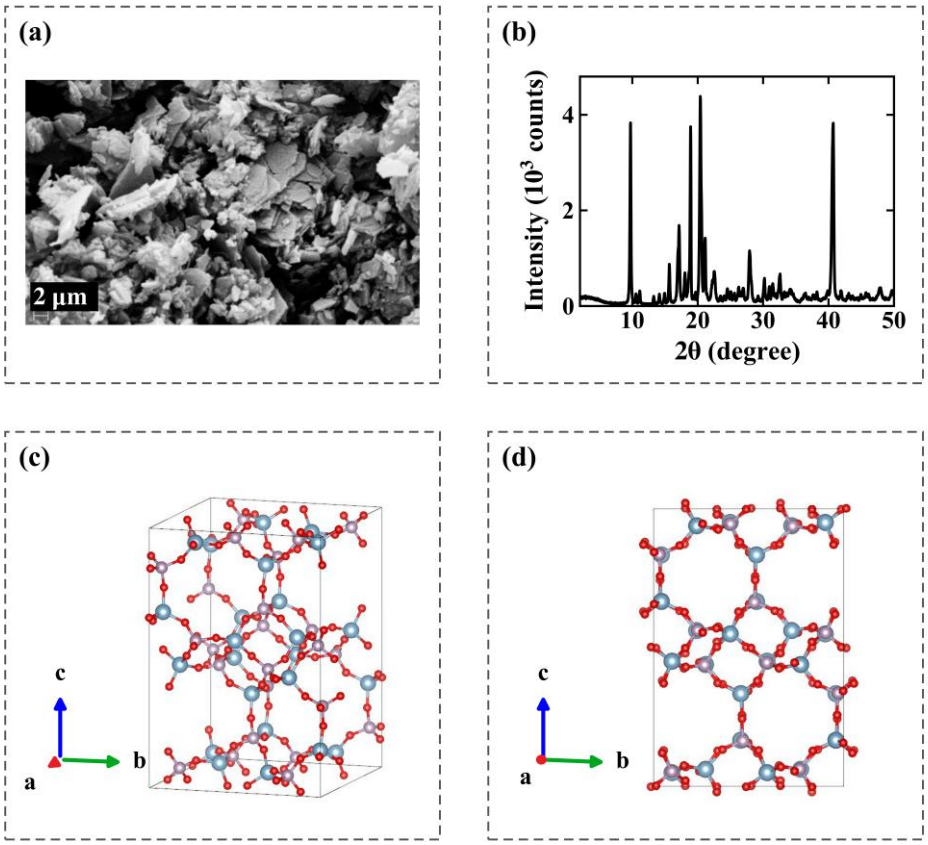


Fig. 1 Morphology, diffraction, and crystallographic views of AlPO-18. (a) Plate-like crystallites and aggregates in the micrometre range. (b) Powder-diffraction intensity of the AEI phase. (c,d) Calcined C2/c framework viewed along two crystallographic directions, showing alternating AlO_4 and PO_4 tetrahedra and the eight-membered-ring channel system. Structural cell data follow the AlPO-18 refinement and IZA reference entry [6,7,19].

2. Methods

The crystallographic reference was the calcined AlPO-18 entry for framework type AEI [6,7]. The conventional C2/c cell has composition $Al_{24}P_{24}O_{96}$, lattice parameters a = 13.7114 Å, b = 12.7315 Å, c = 18.5706 Å, β = 90.01°, and 144 atoms. Its volume was calculated from Eq. (1), giving 3241.81 Å³. Transformation to the

primitive cell halves both the atom count and volume, producing $Al_{12}P_{12}O_{48}$, 72 atoms, and V = 1620.90 Å³. The average Cmcm cell used in the variable-temperature diffraction refinement was retained for comparison with the reported thermal-expansion data [12]; results from the two settings were not mixed in a single normalization.

$$V = abc \sin\beta \tag{1}$$

The elastic tensor was taken from the periodic PBEsol calculation for anhydrous AlPO-18 [17]. The 6 × 6 matrix was symmetrized according to Eq. (2) before diagonalization. Mechanical stability was assessed from the complete eigenvalue spectrum rather than the diagonal elements alone. Reuss bulk, shear, and Young moduli were evaluated from the compliance matrix defined in Eq. (3). The resulting tensor and scalar moduli are reported with three significant figures, commensurate with the precision of the underlying calculation.

$$C_{\mathrm{sym}} = \frac{C + C^{T}}{2} \tag{2}$$

$$S = C_{\mathrm{sym}}{}^{-1} \tag{3}$$

Variable-temperature lattice parameters and volumes were analyzed over 105–455 K using the AlPO-18 diffraction refinements [12]. The fitted volume is given by Eq. (4), with V in Å³ and T in K. The macroscopic volumetric coefficient and the directional coefficients were calculated from Eqs. (5) and (6), respectively, and the directional sum was checked against α_V. A crossover was defined as a zero of $\alpha_V(T)$ within the analyzed interval. Local T···T separations across eight crystallographically distinct T–O–T bridges and the eight-ring span were read on the same temperature scale to identify the linkage motions accompanying the cell contraction.

$$V(T) = 3273.131 - 0.10867T + 3.98137 \times 10^{-5}T^{2} \tag{4}$$

$$\alpha_V(T) = \frac{1}{V(T)}\frac{dV(T)}{dT} \tag{5}$$

$$\alpha_i(T) = \frac{1}{l_i(T)}\frac{dl_i(T)}{dT} \tag{6}$$

The harmonic spectrum was evaluated for the 72-atom primitive framework, giving 216 branches. A valence-force calculation included Al–O and P–O stretching constants of 20 and 40 eV Å⁻², O–Al–O and O–P–O bending constants of 2.5 and 3.5 eV rad⁻², and an Al–O–P hinge constant of 0.40 eV rad⁻². Frequencies were followed along Γ–Y–M–A–Γ, and the density of states was integrated on an 8 × 8 × 8 reciprocal-space mesh. The Raman trace was placed on the same figure using the normalized AlPO-18 spectrum calculated with PBE-D3(BJ) in the spectroscopic study of Airi et al. [18]. Raman intensity and vibrational density of states were kept distinct because they weight normal modes by different observables.

Charge redistribution was evaluated from Eq. (7), where the second term is the superposition of neutral-atom densities at the crystal positions. The two-dimensional sections use red for accumulation, blue for depletion, and green for the zero level. Interpretation was restricted to the sign and spatial topology of Δρ; no integrated charge or Bader population was inferred from the colour map. The accompanying ball-and-stick view uses the calcined IZA coordinates and fixes the location of the displayed density sections within the AEI cage.

$$\Delta\rho(r) = \rho_{\mathrm{AlPO-18}}(r) - \sum_i \rho_i(r) \tag{7}$$

For the mode-resolved expansion analysis, 216 branches were sampled at 36 reciprocal-space points, yielding 7776 mode entries. Frequencies were evaluated at $V_- = 0.995V0$, V_0, and $V_+ = 1.005V0$. The finite-difference Grüneisen parameter and participation ratio were calculated from Eqs. (8) and (9).

$$\gamma(q,\nu) = -\frac{\ln[\omega(q,\nu;V_+)] - \ln[\omega(q,\nu;V_-)]}{\ln(V_+) - \ln(V_-)} \tag{8}$$

$$\mathrm{PR}(q,\nu) = \frac{[\sum_i |e_i(q,\nu)|^2]^2}{N\sum_i |e_i(q,\nu)|^4} \tag{9}$$

The heat-capacity-weighted volumetric contribution was obtained from Eq. (10) using the primitive volume 1620.90 Å³ and the Reuss bulk modulus 73.56 GPa. The spectrum was divided at 3.0 and 8.7 THz to separate collective framework motion, mixed bending motion, and predominantly internal tetrahedral vibration. This calculation tests the frequency weighting required for contraction; the diffraction derivative remains the macroscopic reference.

$$\alpha_V(T) = \frac{1}{BV}\sum_{q\nu} C_{V,q\nu}(T)\gamma_{q\nu} \tag{10}$$

The thermal-transport analysis retains the population and coherence channel decomposition in Eq. (11) [15,16]. Three archived conductivity values were audited independently. The periodic Wigner total is a bulk x-direction

value containing both channels. The Monte Carlo target is a population-only reservoir value. The platelet asymptote belongs to the boundary calculation and its stated branch direction. Their numerical difference was calculated only after the operator, geometry, direction, and channel content had been recorded.

$$\kappa = \kappa_P + \kappa_C \tag{11}$$

The Monte Carlo implementation was validated with a one-dimensional gray two-stream problem before the boundary calculations. Hot and cold reservoirs were separated by L, the intrinsic mean free path was Λ, and the dimensionless length was defined by Eq. (12). For fully thermalizing contacts, the exact gray result is Eq. (13). Twenty-four statistically independent runs were performed for each particle count from 10^2 to 10^5 histories. The relative run-to-run standard deviation was fitted on logarithmic axes and compared with the independent-sampling relation in Eq. (14). Length convergence was accepted according to Eq. (15) [21–24].

$$d = \frac{L}{\Lambda} \tag{12}$$

$$\frac{\kappa_{eff}}{\kappa_{bulk}} = \frac{d}{d+2} \tag{13}$$

$$\sigma_{rel} \propto N^{-1/2} \tag{14}$$

$$\left|\frac{\kappa_{eff}}{\kappa_{bulk}} - 1\right| \leq 0.02 \tag{15}$$

Boundary suppression was evaluated with a prescribed cumulative mean-free-path spectrum in which 90% of the population contribution lies below 18 nm. Platelet thicknesses from 20 to 1000 nm and lateral sizes from 0.1 to 10 μm were examined for specularity p = 0, 0.5, and 0.9. Normalized conductivities were used so that the calculation quantified boundary retention independently of the disputed absolute baselines. The final transient comparison used the AlPO-18/PVOH coating data for 440, 600, and 760 μm layers on aluminium supports [20]. Peak power and temperature were extracted from the same time window and were treated as coupled adsorption-layer responses, not as intrinsic lattice conductivities.

3. Results and Discussion

The SEM image in Fig. 1a shows plate-like AlPO-18 crystallites intergrown into aggregates with lateral dimensions of roughly 0.3–3 μm. The diffraction trace in Fig. 1b retains the characteristic low-angle AEI reflections and the intense group between approximately 16° and 22°, confirming that the open framework rather than a dense aluminophosphate phase controls the structural response. The two crystal views expose the relevant mechanical feature: each oxygen links one AlO_4 and one PO_4 tetrahedron, so an Al–O–P angular displacement can change the projected T···T distance without requiring comparable Al–O or P–O bond compression.

The corrected cell normalization follows directly from this structure. The C2/c conventional cell contains 144 atoms and occupies 3241.81 Å³, whereas the primitive 72-atom cell occupies 1620.90 Å³. A value near 304 Å³ is incompatible with both cells and is smaller than the volume enclosed by an 11.4 Å sphere. All per-volume quantities in the present analysis use the explicit cell in which they were calculated. This correction changes the bookkeeping, not the topology or the diffraction-derived thermal expansion.

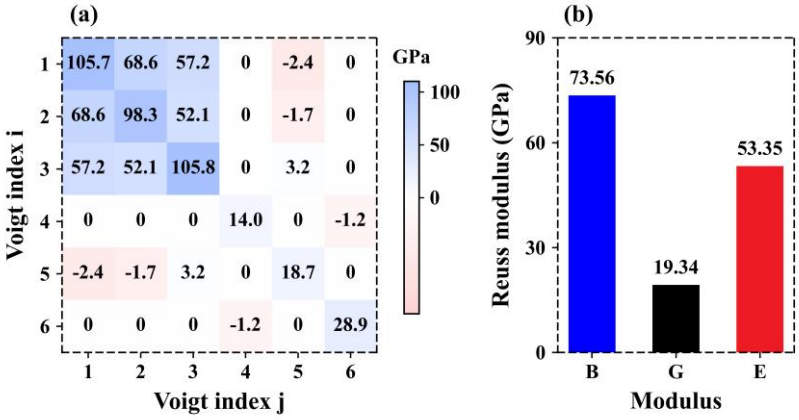


Fig. 2 Calculated elastic response of anhydrous AlPO-18. (a) Symmetrized stiffness tensor C_{ij} in GPa. (b) Reuss bulk (B), shear (G), and Young (E) moduli. Numerical values are taken from the PBEsol elastic calculation for AlPO-18 [17].

All six eigenvalues of the tensor in Fig. 2a are positive: 13.9, 18.2, 29.0, 33.2, 55.0, and 222 GPa. The factor-of-16 span is more informative than any single diagonal term. It shows that the framework combines soft collective strain coordinates with a stiff longitudinal response while remaining mechanically stable. The Reuss values are B_R = 73.56 GPa, G_R = 19.34 GPa, and E_R = 53.35 GPa, with B/G = 3.80. This combination is consistent with angular accommodation in an open network; it does not require weak tetrahedral bonds. The corrected crystallographic and elastic quantities are consolidated in Table 1.

Table 1 Crystallographic normalization and calculated elastic response

Quantity	Value	Unit	Quantity	Value	Unit
Conventional atoms	144	—	Primitive atoms	72	—
a	13.7114	Å	b	12.7315	Å
c	18.5706	Å	β	90.01	degree
V_{conv}	3241.81	Å³	V_{prim}	1620.90	Å³
$\lambda_{min}(C)$	13.9	GPa	$\lambda_{max}(C)$	222	GPa
B_R	73.56	GPa	G_R	19.34	GPa
E_R	53.35	GPa	B/G	3.80	—

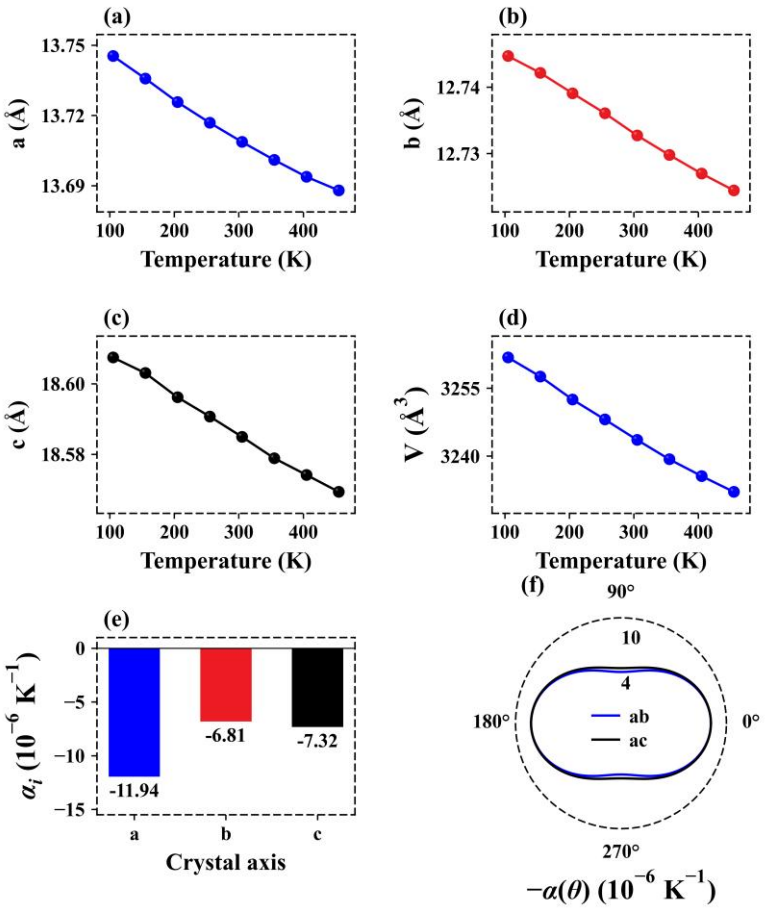


Fig. 3 Temperature dependence of the AlPO-18 lattice. (a–c) Refined a, b, and c parameters. (d) Conventional-cell volume. (e) Directional linear-expansion coefficients. (f) Polar plot of the in-plane expansion response. Data are derived from variable-temperature diffraction refinements [12].

Each lattice parameter in Fig. 3 decreases with temperature. The directional coefficients are -11.94×10^{-6} K^{-1} along a, -6.81×10^{-6} K^{-1} along b, and -7.32×10^{-6} K^{-1} along c. Their sum, -26.07×10^{-6} K^{-1}, agrees with the independently differentiated volume within the precision of the fits. Contraction is strongest along a but remains negative along all three crystallographic directions; the polar curves therefore describe an anisotropic magnitude rather than a competition between positive and negative axes.

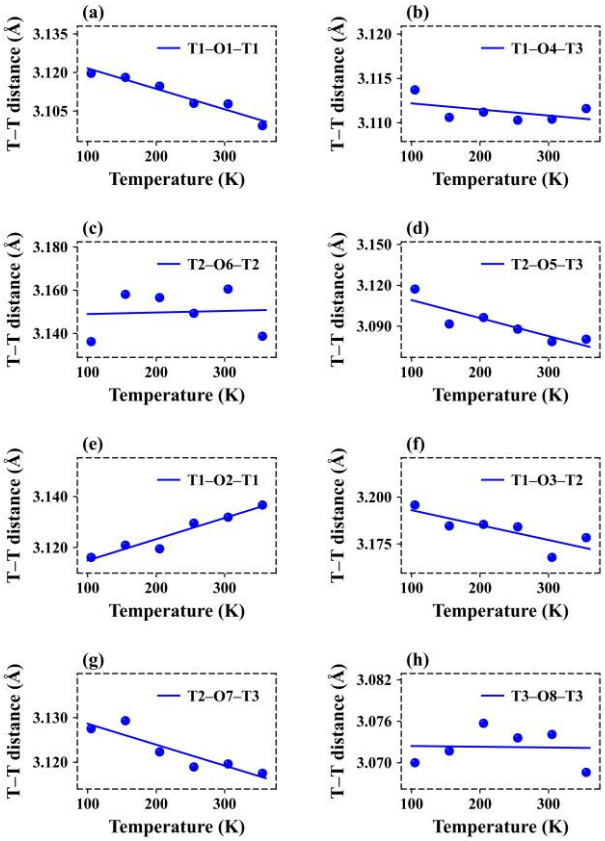


Fig. 4 Temperature evolution of eight T···T separations across crystallographically distinct T–O–T bridges in AlPO-18. Lines are linear trends through the refined distances [12].

The local distances in Fig. 4 rule out uniform bond contraction as the sole explanation. Five bridges contract clearly, two are nearly temperature independent, and T_1–O_2–T_1 expands slightly. The largest decreases occur for T_1–O_1–T_1, from about 3.121 to 3.100 Å, and T_2–O_5–T_3, from about 3.116 to 3.078 Å over 105–355 K. By contrast, T_2–O_6–T_2 remains close to 3.15 Å and T_3–O_8–T_3 stays near 3.072 Å. The coexistence of contracting, invariant, and weakly expanding local spans is the geometric signature of cooperative hinging: the unit cell contracts through correlated angular changes rather than a common decrease in every nearest-neighbour distance.

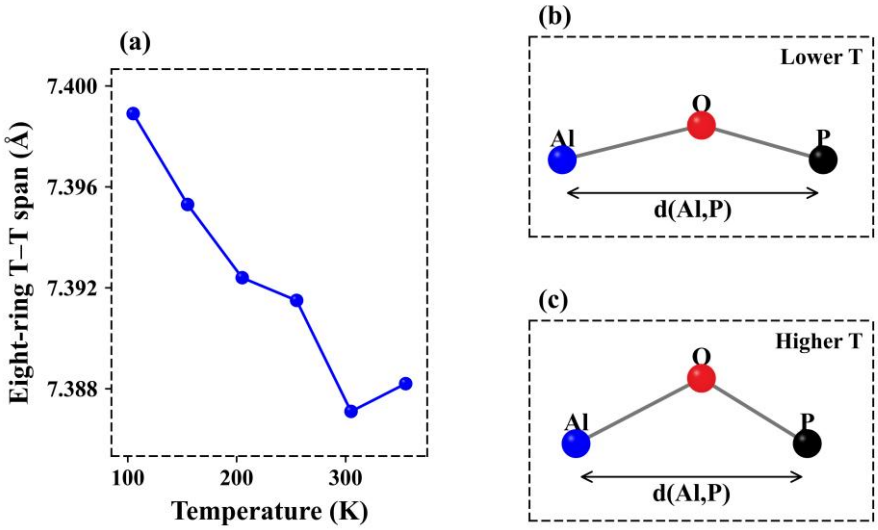


Fig. 5 Eight-ring contraction and Al–O–P hinge geometry. (a) Temperature-dependent T···T span across the eight-membered-ring window. (b,c) Transverse displacement of the bridging oxygen reduces the projected Al···P distance as temperature increases [12].

The eight-ring span provides a collective measure of the same mechanism. It decreases from approximately 7.399 Å at 105 K to 7.387 Å at 305 K, a contraction of 0.012 Å or 0.16%, before a small recovery to 7.388 Å at 355 K. The sketches in Fig. 5b,c show why the Al···P projection shortens when oxygen moves transverse to the line joining the tetrahedral centres. A change of bridge angle is energetically cheaper than a comparable change in the internal P–O stretch, so the low-frequency transverse coordinate carries a negative strain response while the tetrahedra remain locally intact.

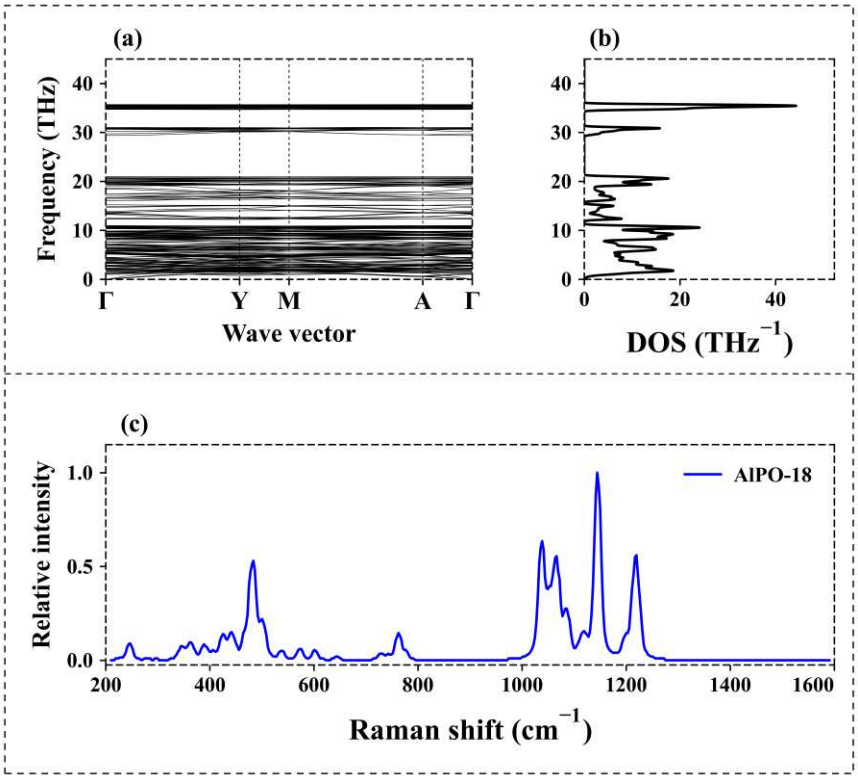


Fig. 6 Vibrational response of AlPO-18. (a) Harmonic dispersion along Γ–Y–M–A–Γ for the 216-branch primitive-cell calculation. (b) Vibrational density of states from the 8 × 8 × 8 mesh. (c) Normalized AlPO-18 Raman response on a wavenumber scale [18].

The 216 branches in Fig. 6a are a direct consequence of the 72-atom primitive cell. Acoustic branches emerge from Γ, but a dense set of weakly dispersive framework modes enters immediately above them. The density of states is concentrated below approximately 20 THz, with smaller high-frequency groups near 30–36 THz. In the Raman spectrum, the strongest intensities occur near 500 cm⁻¹ and across 1050–1250 cm⁻¹. These peaks should not be read as heat-current weights: Raman intensity follows the polarizability derivative, whereas thermal transport depends on velocity, lifetime, and the heat-current operator. The spectral separation nonetheless supports the structural assignment. Low-frequency modes are dominated by collective framework bending and rotation, while the upper Raman group is associated mainly with internal tetrahedral stretching.

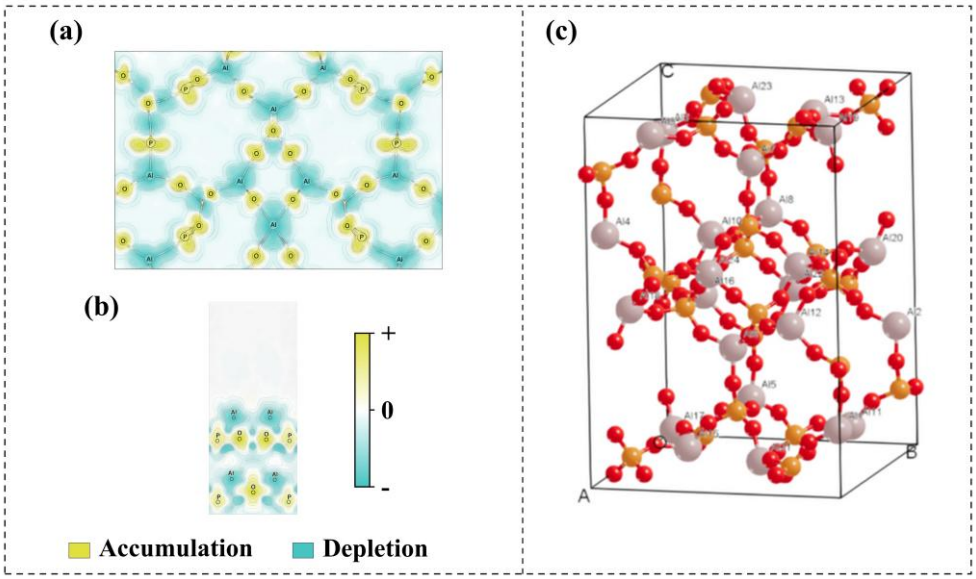


Fig. 7 Charge redistribution and structural context in calcined AlPO-18. (a,b) Two density-difference sections, with red/yellow indicating accumulation, blue/cyan depletion, and green the zero region. (c) C2/c framework showing the Al–O–P linkage network sampled by the sections.

The density-difference sections in Fig. 7 show accumulation concentrated around oxygen and along the P–O region, together with depletion around the more electropositive centres. This spatial separation is consistent with a stiff internal tetrahedral stretch and a more compliant intertetrahedral angle. The figure is used for bonding topology rather than charge quantification: the red and blue regions identify where density is rearranged, while the crystal view locates those regions within the continuous cage wall. The result explains how low-energy hinge motion can coexist with positive elastic eigenvalues and high-frequency P–O Raman bands.

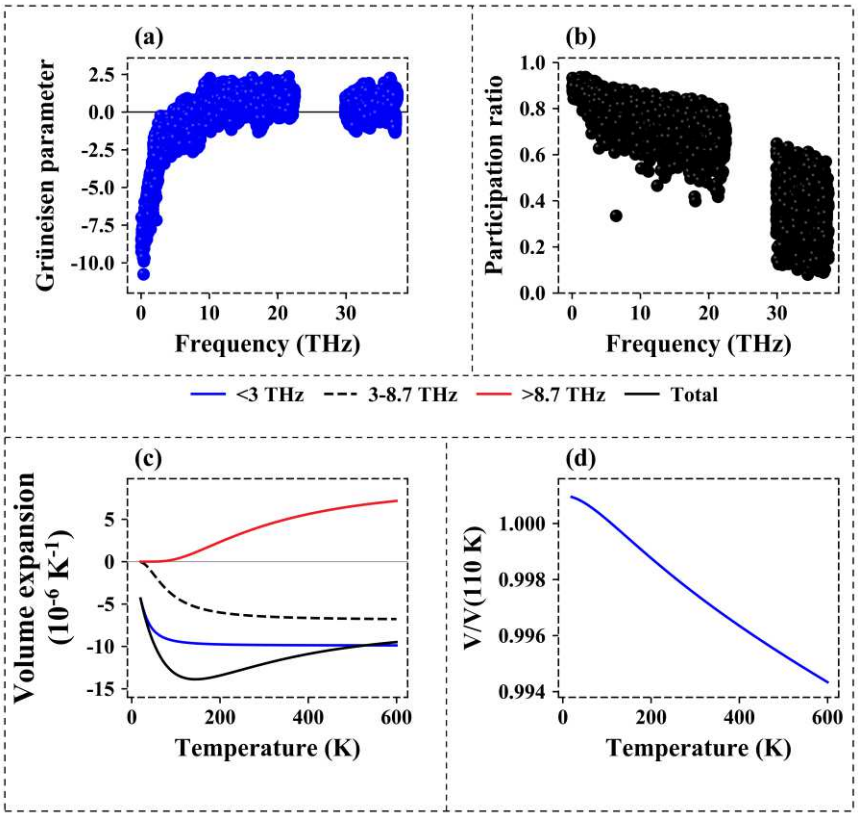


Fig. 8 Mode-resolved expansion analysis. (a) Grüneisen parameters for 7776 mode entries. (b) Participation ratios on the same frequency scale. (c) Heat-capacity-weighted volumetric contributions below 3 THz, from 3 to 8.7 THz, above 8.7 THz, and their sum. (d) Integrated relative volume normalized at 110 K.

The mode population in Fig. 8a spans $\gamma = -10.76$ to 2.37. The strongest negative values are confined to the lowest-frequency sector, whereas most modes above 8.7 THz are weakly positive. Participation ratios range from 0.080 to 0.937. Low-frequency negative modes retain relatively high participation, so the contractive

response is collective rather than the consequence of isolated local defects. At 300 K, modes below 3 THz contribute -9.84×10^{-6} K^{-1}, the 3–8.7 THz interval contributes -6.47×10^{-6} K^{-1}, and the upper sector contributes $+4.25 \times 10^{-6}$ K^{-1}. Their sum is -12.05×10^{-6} K^{-1}. The sign agrees with diffraction, while the smaller magnitude shows the sensitivity of a modal sum to its force constants, elastic normalization, and spectral sampling. For that reason, the macroscopic claim is based on the differentiated diffraction volume in Fig. 9 rather than the sign of selected γ values alone.

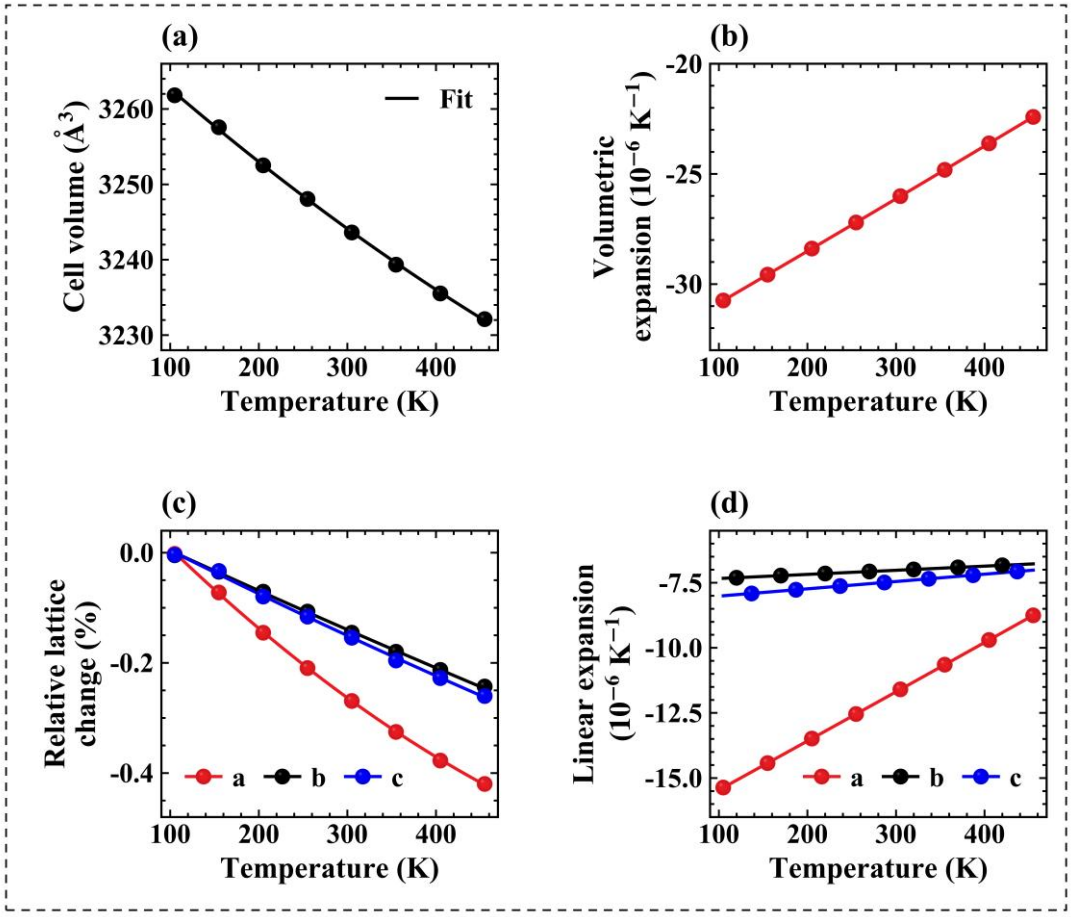


Fig. 9 Macroscopic negative thermal expansion of AlPO-18. (a) Conventional-cell volume and quadratic fit. (b) Volumetric expansion coefficient obtained by differentiating the fitted volume. (c) Relative changes of a, b, and c. (d) Corresponding linear-expansion coefficients [12].

Figure 9 establishes the bulk response required by the thermal-expansion claim. The refined volume decreases from 3261.80 to 3232.11 Å³ between 105 and 455 K, corresponding to a 0.91% contraction. Differentiation of the quadratic fit gives $\alpha_V = -30.75 \times 10^{-6}$ K^{-1} at 105 K, -26.18×10^{-6} K^{-1} at 298 K, and -22.41×10^{-6} K^{-1} at 455 K. The coefficient remains negative across the complete interval; the formal zero of the derivative lies far outside it, so there is no crossover between 105 and 455 K. The monotonic decrease in $|\alpha_V|$ reflects increasing positive weight from higher-frequency modes, consistent with the spectral decomposition in Fig. 8c, but it is insufficient to reverse the framework contraction, values are summarized in Table. 2.

Table 2 Fitted AlPO-18 volume and volumetric thermal-expansion coefficient

T (K)	V_{fit} (Å³)	α_V (10^{-6} K^{-1})
105	3262.160	-30.75
155	3257.244	-29.57
205	3252.527	-28.39
255	3248.009	-27.21
305	3243.690	-26.01
355	3239.571	-24.82
405	3235.650	-23.62

T (K)	V_{fit} (Å³)	α_V (10^{-6} K^{-1})
455	3231.929	-22.41

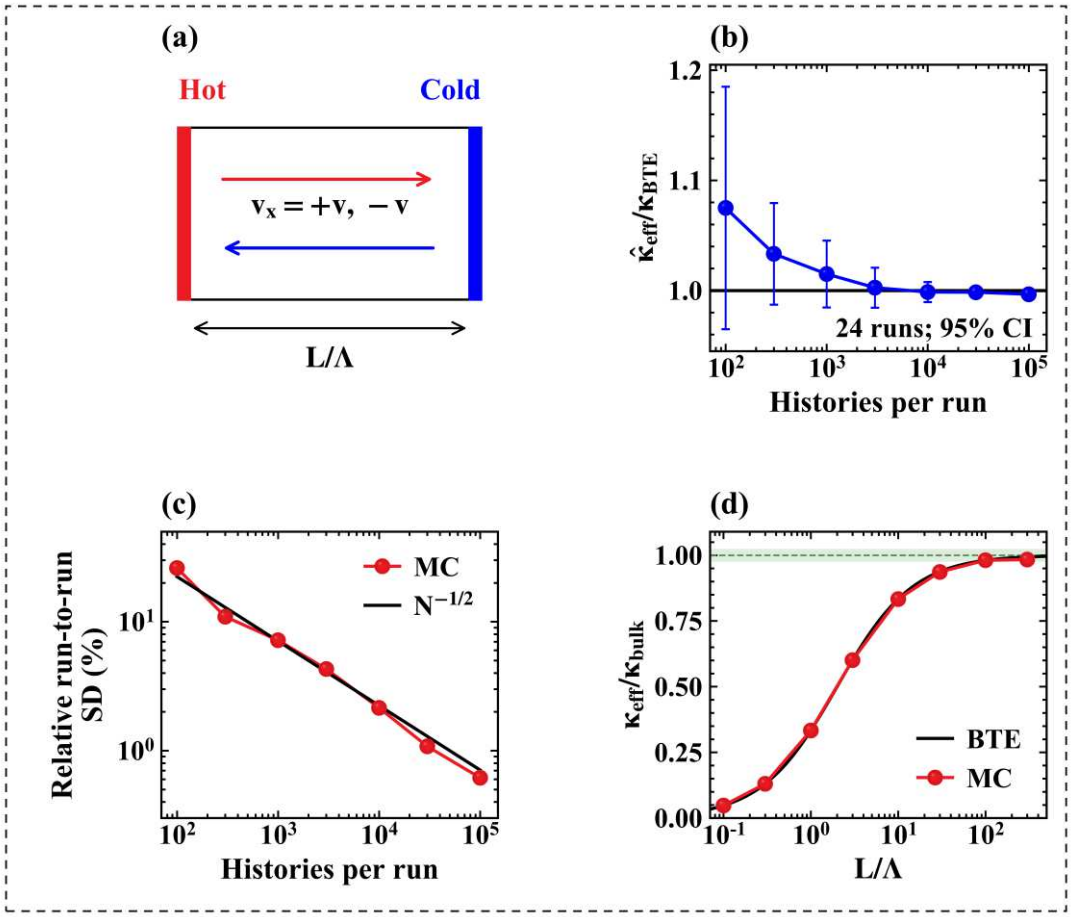


Fig. 10 Deviational Monte Carlo validation in the gray two-stream limit. (a) Reservoir geometry. (b) Normalized conductivity versus histories per run for 24 replicas. (c) Relative run-to-run standard deviation and N−1/2 reference. (d) Recovery of the diffusive BTE limit as L/Λ increases [24].

The validation in Fig. 10 separates statistical convergence from length convergence. Increasing the histories per run from 10^2 to 10^5 contracts the 24-replica interval without shifting the mean systematically. A log–log fit gives a relative-uncertainty slope of −0.530, close to the independent-sampling value −0.5 in Eq. (14). The length sweep follows the analytic gray solution in Eq. (13). Setting the normalized conductivity to 0.98 gives d = 98, so the 2% diffusive criterion is reached at $L/\Lambda \geq 98$. This result is dimensionless; a length in nanometres is obtained only after assigning the relevant modal mean free path. The benchmark therefore validates the estimator and reservoir treatment without being confused with the absolute AlPO-18 conductivity.

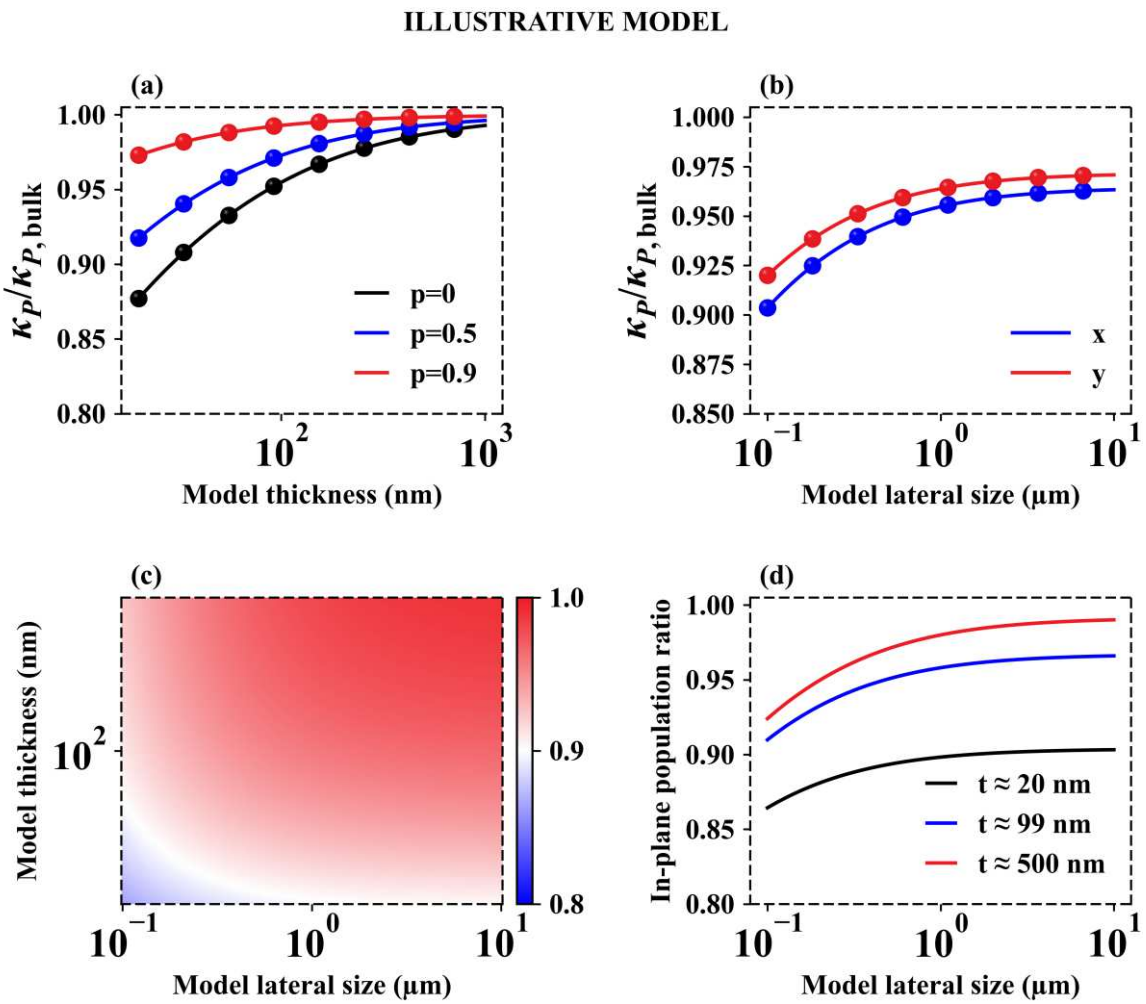


Fig. 11 Normalized boundary response. (a) Thickness dependence for p = 0, 0.5, and 0.9. (b) Directional response to lateral size. (c) Diffuse-boundary map versus thickness and lateral size. (d) In-plane response at selected thicknesses for the prescribed mean-free-path distribution.

Boundary suppression is largest when the thickness overlaps the dominant mean-free-path range. At 20 nm, $\kappa_{eff}/\kappa_{bulk}$ is 0.877 for diffuse faces, 0.917 for p = 0.5, and 0.973 for p = 0.9. At 1000 nm the corresponding ratios rise to 0.9929, 0.9962, and 0.9992. The recovery is therefore controlled more strongly by thickness than by changing the lateral size across 0.1–10 μm. Figure 11c shows the same hierarchy as a steep gradient along the thickness direction and a shallower gradient along the lateral direction. Specularity matters primarily at the smallest thicknesses because repeated face encounters preserve or destroy directional momentum before intrinsic scattering restores the distribution.

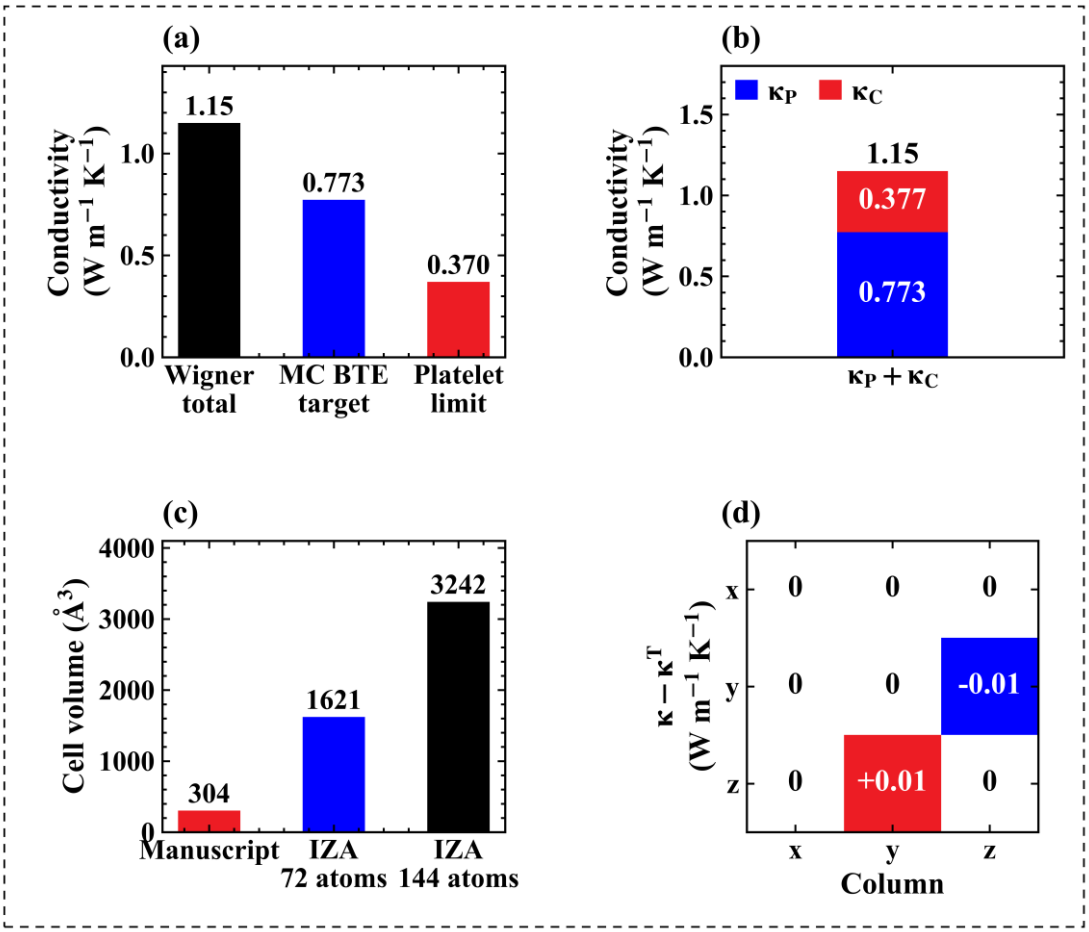


Fig. 12 Numerical consistency of the volume and conductivity baselines. (a) Periodic Wigner total, Monte Carlo BTE target, and platelet limit. (b) Conditional arithmetic split of 1.150 W m^{-1} K^{-1} into 0.773 and 0.377 W m^{-1} K^{-1}. (c) Conventional- and primitive-cell volumes relative to the excluded 304 Å^3 value. (d) Antisymmetric part $\kappa - \kappa^T$ of the archived conductivity tensor.

Figure 12 makes the baseline distinction explicit. The periodic Wigner total is 1.150 W m^{-1} K^{-1}, the Monte Carlo target is 0.773 W m^{-1} K^{-1}, and the platelet limit is 0.370 W m^{-1} K^{-1}. These values differ because the calculations use different transport operators and geometries. If 0.773 W m^{-1} K^{-1} were imposed as the population part of the same periodic x-direction Wigner result, the arithmetic residual would be 0.377 W m^{-1} K^{-1}, or 32.8% of the total. The present analysis does not use that residual as an independently calculated coherence conductivity, because the Monte Carlo target is a reservoir operator rather than the population block of the periodic Wigner tensor. The distinction removes the need to force three physically different baselines onto one curve.

The volume panel records the corrected 1620.90 and 3241.81 Å^3 cells and excludes 304 Å^3 from every normalization. The tensor audit also identifies $\kappa_{yz} - \kappa_{zy} = -0.01$ W m^{-1} K^{-1} and $\kappa_{zy} - \kappa_{yz} = +0.01$ W m^{-1} K^{-1} in the archived rounded entries. Thermal-conductivity reciprocity requires the symmetric part, so the antisymmetric residual is removed before reporting the diagonal tensor. Table 3 assigns each conductivity to its operator, geometry, axis, and channel content; the table, rather than a qualitative explanation, is the reference for cross-comparison.

Table 3 Reconciliation of room-temperature conductivity baselines

Operator	Geometry	Axis	Channel	κ (W m^{-1} K^{-1})
Periodic Wigner	Periodic bulk	x	P + C	1.150
MC BTE target	1D reservoirs	x	P	0.773
Conditional residual	Arithmetic match	x	C	0.377
Platelet limit	Finite platelet	z branch	Boundary	0.370

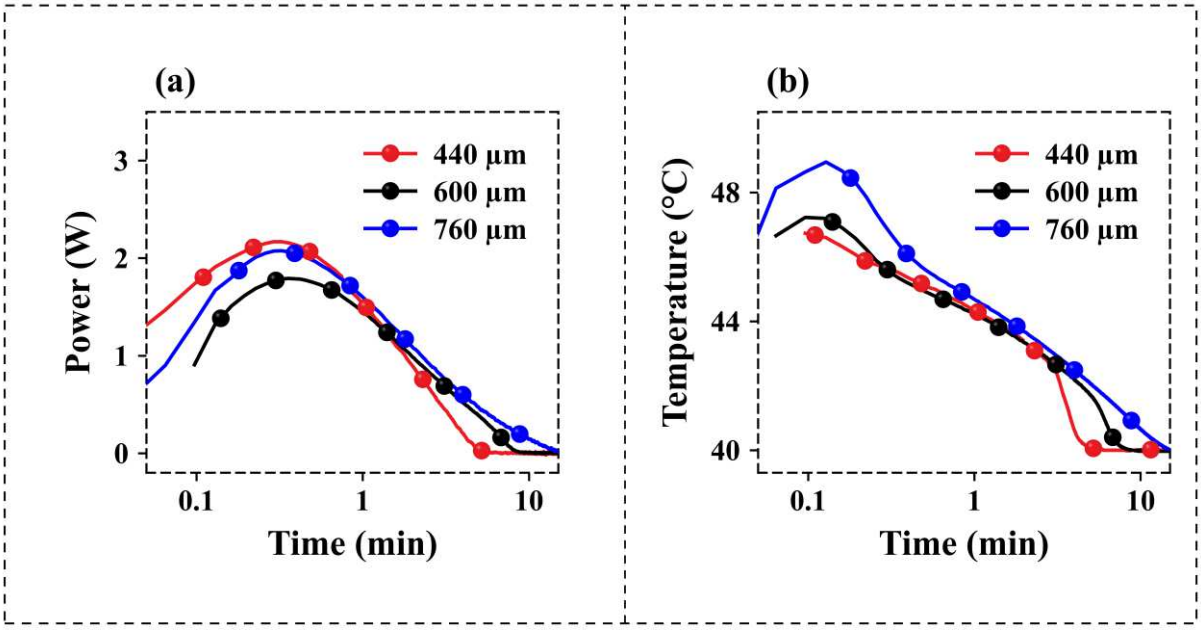


Fig. 13 Transient response of AlPO-18/PVOH coatings on aluminium supports. (a) Thermal power and (b) coating temperature for thicknesses of 440, 600, and 760 µm [20].

The coating traces in Fig. 13 provide the application-scale endpoint. Peak powers are 2.17, 1.79, and 2.08 W for the 440, 600, and 760 µm layers, respectively, while the maximum temperatures are 46.7, 47.2, and 48.9 °C. The thickest layer stores more active material and reaches the highest temperature, but its power does not increase monotonically because heat release, vapour transport, and thermal resistance evolve simultaneously. All three curves decay toward zero power over roughly 10 min as the coatings approach equilibrium. These values characterize the composite layer and aluminium support; they are not substitutes for the periodic lattice conductivity.

The combined results give a continuous, quantitatively constrained account of AlPO-18. Positive elastic eigenvalues establish mechanical stability, while the anisotropic negative lattice derivatives establish macroscopic contraction. The mixed signs of individual T⋯T distances and the 0.012 Å decrease of the eight-ring span locate the response in cooperative hinge motion. Low-frequency negative Grüneisen values then supply a vibrational counterpart, with positive high-frequency contributions reducing but not reversing α_V over 105–455 K. At larger scales, the gray Monte Carlo benchmark verifies statistical and diffusive convergence, the platelet calculation isolates the effect of surface encounters, and the coating data reveal the additional thermal resistance introduced by a real composite geometry.

The novelty lies in this consistency chain rather than in treating every plotted quantity as the output of one operator. Cell volume is tied to atom count; the sign of expansion is tied to $\alpha_V(T)$; a modal decomposition is checked against diffraction; each conductivity is tied to channel, direction, and boundary condition; and coating transients are kept separate from intrinsic lattice transport. This structure permits direct numerical comparison without conflating crystallographic conventions, transport baselines, or length scales.

4. Conclusions

The results establish AlPO-18 as a mechanically stable yet structurally flexible framework. The calcined conventional C2/c cell contains 144 atoms and has a volume of 3241.81 Å³, while the corresponding 72-atom primitive cell has a volume of 1620.90 Å³. These values provide an unambiguous normalization for all cell-dependent quantities. The elastic tensor is positive definite, with eigenvalues ranging from 13.9 to 222 GPa, and the calculated Reuss bulk modulus is 73.56 GPa. The coexistence of soft collective deformation modes and a mechanically stable tetrahedral skeleton enables the framework to respond to temperature through angular motion rather than extensive Al–O or P–O bond compression.

The macroscopic thermal response is characterized by a 0.91% decrease in conventional-cell volume between 105 and 455 K. Over this interval, the volumetric thermal-expansion coefficient remains negative, changing from -30.75×10^{-6} K^{-1} at 105 K to -22.41×10^{-6} K^{-1} at 455 K, with $\alpha_V(298\ \text{K}) = -26.18 \times 10^{-6}$ K^{-1}. No crossover is observed within the investigated temperature range. The directional coefficients along the a, b, and c axes are −11.94, −6.81, and -7.32×10^{-6} K^{-1}, respectively, demonstrating that the contraction is anisotropic

but occurs along all three crystallographic directions. The temperature dependence of the local T⋯T separations and the eight-membered-ring span identifies transverse Al–O–P hinging and cooperative ring closure as the principal structural origin of this behaviour.

The vibrational results support the structural interpretation. The most negative Grüneisen parameters occur within the low-frequency region and are associated with modes having relatively high participation ratios, confirming that the contraction originates from collective framework motion rather than isolated local vibrations. At 300 K, modes below 3 THz and between 3 and 8.7 THz contribute −9.84 and −6.47 × 10^{-6} K^{-1}, respectively, whereas modes above 8.7 THz contribute +4.25 × 10^{-6} K^{-1}. The resulting modal sum of −12.05 × 10^{-6} K^{-1} reproduces the sign of the macroscopic response, although its smaller magnitude demonstrates the sensitivity of mode-resolved expansion to the force constants, elastic normalization, and reciprocal-space sampling. The diffraction-derived coefficient therefore provides the reference value for the bulk response.

The transport analysis reconciles the three reported conductivity baselines by assigning each value to its corresponding operator and geometry. The periodic Wigner total is 1.150 W m^{-1} K^{-1}, the reservoir Monte Carlo population target is 0.773 W m^{-1} K^{-1}, and the boundary-limited platelet value is 0.370 W m^{-1} K^{-1}. These values describe different transport conditions and should not be interpreted as competing estimates of a single bulk conductivity. The Monte Carlo benchmark follows an $N^{-0.53}$ statistical scaling and approaches the gray diffusive limit within 2% when $L/\Lambda \geq 98$. For the prescribed mean-free-path distribution, reducing the platelet thickness to 20 nm lowers the normalized conductivity to 0.877 for diffuse boundaries, whereas a specularity of $p = 0.9$ retains a value of 0.973. The AlPO-18/PVOH coating response further shows that application-scale power and temperature depend on coupled heat and mass transfer in addition to intrinsic lattice transport. Together, these results connect framework dynamics, macroscopic thermal response, and geometry-dependent heat transport, providing a consistent basis for evaluating AlPO-18 in heat-transformation applications.

References

1. W. Yan, X. Song,, R. Xu, Molecular engineering of microporous crystals: (I) New insight into the formation process of open-framework aluminophosphates, Microporous and Mesoporous Materials, vol. 123, no 1-3, p. 50-62, juill. 2009. https://doi.org/10.1016/j.micromeso.2009.03.023
2. Y. Hao, al., Design, Synthesis, and Improvement of Nonlinear Optical Properties from Aluminophosphite to Aluminophosphate, Inorg. Chem., vol. 64, no 27, p. 13805-13814, juill. 2025. https://doi.org/10.1021/acs.inorgchem.5c01496
3. Y. Du, P. A. Wright, Aluminophosphate Zeotypes: Structural Chemistry and Applications, in Zeolites, D. P. Serrano, J. Čejka, Éd., Royal Society of Chemistry, 2025, p. 155-196. https://doi.org/10.1039/9781837676859-00155
4. B. Wang, F. Gao, F. Zhang, W. Xing,, R. Zhou, Highly permeable and oriented AlPO-18 membranes prepared using directly synthesized nanosheets for CO_2 /CH_4 separation, J. Mater. Chem. A, vol. 7, no 21, p. 13164-13172, 2019. https://doi.org/10.1039/C9TA01233H
5. Z. Zong, S. K. Elsaidi, P. K. Thallapally,, M. A. Carreon, Highly Permeable AlPO-18 Membranes for N_2 /CH_4 Separation, Ind. Eng. Chem. Res., vol. 56, no 14, p. 4113-4118, avr. 2017. https://doi.org/10.1021/acs.iecr.7b00853
6. A. Simmen, L. B. McCusker, Ch. Baerlocher, W. M. Meier, The structure determination and Rietveld refinement of the aluminophosphate $AlPO_4$-18, Zeolites 11 (1991) 654–661. https://doi.org/10.1016/S0144-2449(05)80167-8
7. International Zeolite Association Structure Commission, Database of Zeolite Structures, AEI framework and calcined AlPO-18 reference material. https://www.iza-structure.org/databases/ (accessed 29 October 2026).
8. Md. Mohiuddin, M. M. Hasan,, A. Kabir, Stability Analysis and Optoelectronic Properties of Mg_3 ZBr_3 (Z = As, Sb, Bi) Perovskites for Evaluating the Performance in PIN Photodiodes, ACS Omega, p. acsomega.5c11440, févr. 2026. https://doi.org/10.1021/acsomega.5c11440
9. A. Shaikh, J. Wu,, B. Peng, Negative and Positive Anisotropic Thermal Expansion in 2D Fullerene Networks, Phys. Rev. Lett., vol. 135, no 12, p. 126103, sept. 2025. https://doi.org/10.1103/tck2-78dx
10. W. Huang, Y. Li,, D. Yang, Local Bond Engineering in $LiMBO_4$ (M = Si, Ge): Synergistic Negative Grüneisen Parameter and Bond Stiffening for Reduced Thermal Expansion, Chem. Mater., vol. 38, no 4, p. 1766-1775, févr. 2026. https://doi.org/10.1021/acs.chemmater.5c02627
11. Z. Tang, al., Effects of thermal expansion and four-phonon interactions on the lattice thermal conductivity of the negative thermal expansion material ScF_3, Phys. Rev. B, vol. 110, no 13, p. 134320, oct. 2024. https://doi.org/10.1103/PhysRevB.110.134320
12. M. Amri, R. I. Walton, Negative Thermal Expansion in the Aluminum and Gallium Phosphate Zeotypes with CHA and AEI Structure Types, Chem. Mater. 21 (2009) 3380–3390. https://doi.org/10.1021/cm901140u
13. H. Sun, T. Wang, Z. Ju, D. Ma, J. Zhou,, L. Zhang, Line Width-Activated Interband Contribution to Thermally Driven Phonon Angular Momentum, Nano Lett., vol. 26, no 22, p. 7339-7346, juin 2026. https://doi.org/10.1021/acs.nanolett.6c01041
14. N. G. Erhardt, al., Electron-mediated anharmonicity and its role in the Raman spectrum of graphene, npj Comput Mater, vol. 11, no 1, p. 114, avr. 2025. https://doi.org/10.1038/s41524-025-01610-9
15. M. Simoncelli, N. Marzari,, F. Mauri, Wigner Formulation of Thermal Transport in Solids, Phys. Rev. X, vol. 12, no 4, p. 041011, oct. 2022. https://doi.org/10.1103/PhysRevX.12.041011

16. Z. Ju, Z. Chang, N. Xiao, X. Qian, Y. Zhou,, D. Ma, Lattice thermal conductivity of Li Nb O $_3$ considering high-order anharmonicity and phonon mutual coherence channel, Phys. Rev. Applied, vol. 24, no 2, p. 024035, août 2025. https://doi.org/10.1103/gp7t-klvy
17. F. Colmenero, Á. Lobato, V. Timón, Mechanical Characterization of Anhydrous Microporous Aluminophosphate Materials: Tridimensional Incompressibility, Ductility, Isotropy and Negative Linear Compressibility, Solids 3 (2022) 457–499. https://doi.org/10.3390/solids3030032
18. A. Airi, A. Damin, J. Xie, U. Olsbye, S. Bordiga, Catalyst sites and active species in the early stages of MTO conversion over cobalt AlPO-18 followed by IR spectroscopy, Catal. Sci. Technol. 12 (2022) 2775–2792. https://doi.org/10.1039/D2CY00303A
19. L. D. Anbealagan, T. L. Chew, Y. F. Yeong, Z. A. Jawad, C. D. Ho, Synthesis and characterization of (3-aminopropyl) triethoxysilane (APTES) functionalized zeolite AlPO-18, IOP Conf. Ser.: Mater. Sci. Eng. 1195 (2021) 012047. https://doi.org/10.1088/1757-899X/1195/1/012047
20. H. van Heyden, G. Munz, L. Schnabel, F. Schmidt, S. Mintova, T. Bein, Kinetics of water adsorption in microporous aluminophosphate layers for regenerative heat exchangers, Appl. Therm. Eng. 29 (2009) 1514–1522. https://doi.org/10.1016/j.applthermaleng.2008.07.001
21. K. Z. Adnan, T. Feng, Thermal boundary conductance and thermal conductivity strongly depend on nearby environment, Phys. Rev. B, vol. 109, no 24, p. 245302, juin 2024. https://doi.org/10.1103/PhysRevB.109.245302
22. L. G. Fabreti, S. Höhna, Convergence assessment for Bayesian phylogenetic analysis using MCMC simulation, Methods Ecol Evol, vol. 13, no 1, p. 77-90, janv. 2022. https://doi.org/10.1111/2041-210X.13727
23. P. Biswas, J. Lee, A. Roy,, B. Cukurel, Ballistic contributions to mesoscale thermal conductivity: Closing a flux-based model with lattice–Boltzmann–Peierls–Callaway simulations, Journal of Applied Physics, vol. 140, no 4, p. 045103, juill. 2026. https://doi.org/10.1063/5.0332327
24. J.-P. M. Péraud, N. G. Hadjiconstantinou, Efficient simulation of multidimensional phonon transport using energy-based variance-reduced Monte Carlo formulations, Phys. Rev. B 84 (2011) 205331. https://doi.org/10.1103/PhysRevB.84.205331
25. H. Liu, X. Zhao, Thermal Conductivity Analysis of High Porosity Structures with Open and Closed Pores, International Journal of Heat and Mass Transfer, vol. 183, p. 122089, févr. 2022. https://doi.org/10.1016/j.ijheatmasstransfer.2021.122089
26. L. Zhu, S. Wu, C. Zhang, S. Misra, X. Zhou,, J. Cai, Characterization of Pore Electrical Conductivity in Porous Media by Weakly Conductive and Nonconductive Pores, Surv Geophys, vol. 44, no 3, p. 877-923, juin 2023. https://doi.org/10.1007/s10712-022-09761-w
27. J.-B. Kim, al., Anharmonic Phonon Scattering Triggering Multi-ion Migration in Oxide-Based Superionic Conductors, J. Am. Chem. Soc., vol. 147, no 37, p. 33743-33753, sept. 2025. https://doi.org/10.1021/jacs.5c09777
28. K. Ghosh, A. Kusiak,, J.-L. Battaglia, Phonon hydrodynamics in crystalline materials, J. Phys.: Condens. Matter, vol. 34, no 32, p. 323001, août 2022. https://doi.org/10.1088/1361-648X/ac718a
29. X. Qian, C. Zhang, T.-H. Liu,, R. Yang, Analytical Green's function of the multidimensional Boltzmann transport equation for modeling hydrodynamic second sound, Phys. Rev. B, vol. 111, no 3, p. 035406, janv. 2025. https://doi.org/10.1103/PhysRevB.111.035406
30. F. Lebeda, M. Demleitner, A. Pongratz, H. Ruckdäschel,, M. Retsch, Shaping Thermal Transport and Temperature Distribution via Anisotropic Carbon Fiber Reinforced Composites, ACS Omega, vol. 9, no 37, p. 39232-39241, sept. 2024. https://doi.org/10.1021/acsomega.4c06558
31. C. Pei, al., Weakly Anisotropic Superconductivity of $Pr_4 Ni_3 O_{10}$ Single Crystals, J. Am. Chem. Soc., vol. 148, no 1, p. 1388-1396, janv. 2026. https://doi.org/10.1021/jacs.5c17977
32. M. A. García-Blázquez, J. J. Esteve-Paredes, A. J. Uría-Álvarez,, J. J. Palacios, Shift Current with Gaussian Basis Sets and General Prescription for Maximally Symmetric Summations in the Irreducible Brillouin Zone, J. Chem. Theory Comput., vol. 19, no 24, p. 9416-9434, déc. 2023. https://doi.org/10.1021/acs.jctc.3c00917
33. B. Hu, al., Unveiling Microscopic Mechanisms of Chemical Mechanical Polishing via Multi-Scale Theoretical Calculations, J Comput Chem, vol. 46, no 22, p. e70213, août 2025. https://doi.org/10.1002/jcc.70213
34. M. Asle Zaeem, S. Thomas, S. Kavousi, N. Zhang, T. Mukhopadhyay,, A. Mahata, Multiscale computational modeling techniques in study and design of 2D materials: recent advances, challenges, and opportunities, 2D Mater., vol. 11, no 4, p. 042004, oct. 2024. https://doi.org/10.1088/2053-1583/ad63b6
35. P. Ghanizadeh, N. Donmezer, N. Eom,, A. Ahadi, First-principles study of the effects of biaxial tensile strain and size confinement on phonon transport in β -Ga_2O_3, Journal of Applied Physics, vol. 139, no 23, p. 235105, juin 2026. https://doi.org/10.1063/5.0327540
36. D. Vasilyev, Comparison of thermal expansion path of the Fe_2Mo Laves phase calculated using the DFT-based phonon and Debye-Grüneisen approaches, Materials Today Communications, vol. 35, p. 105550, juin 2023. https://doi.org/10.1016/j.mtcomm.2023.105550
37. F. Li, X. Liu, N. Ma, L. Chen,, L. Wu, Thermoelectric Zintl Compound In $_{1-x}$ Ga $_x$ Te: Pure Acoustic Phonon Scattering and Dopant-Induced Deformation Potential Reduction and Lattice Shrink, Angew Chem Int Ed, vol. 61, no 35, p. e202208216, août 2022. https://doi.org/10.1002/anie.202208216
38. H. Guo, J. S. Baker, W. Wu,, K. L. Choy, High Dielectric Constants in $BaTiO_3$ Due to Phonon Mode Softening Induced by Lattice Strains: First Principles Calculations, Advanced Physics Research, vol. 2, no 9, p. 2300001, sept. 2023. https://doi.org/10.1002/apxr.202300001
39. M. Darvish Ganji, M. Rezvani,, H. Ko, Bridging the theoretical gap between electronic structure and dynamic stability: An integrated computational framework for ZnO sheet-based chemical warfare agent sensors, Surfaces and Interfaces, vol. 91, p. 109196, juin 2026. https://doi.org/10.1016/j.surfin.2026.109196
40. S. K. Sahu, S. K. Padhi, R. R. Mohapatra,, P. Padhan, Thermal transport in $SrSnO_3$ revealed by first-principles theory, Raman thermometry and machine learning, J. Mater. Chem. A, vol. 14, no 42, p. 28455-28471, 2026. https://doi.org/10.1039/D6TA02865A
41. A. Cammarata, T. Polcar, Fine control of lattice thermal conductivity in low-dimensional materials, Phys. Rev. B, vol. 103, no 3, p. 035406, janv. 2021. https://doi.org/10.1103/PhysRevB.103.035406

42. D. Demirtürk, H. I. Ozturk,, M. Guler, A comparative analysis of the thermal conductivity measurement of asphalt concrete under steady-state and transient heat transfer conditions, Mater Struct, vol. 59, no 4, p. 194, mai 2026. https://doi.org/10.1617/s11527-026-03091-8